J Solid State Electrochem (2013) 17:1175–1184
DOI 10.1007/s10008-012-1985-z

ORIGINAL PAPER

Photoelectrochemical properties of MoO_2 thin films

Nijolė Dukštienė · Dovilė Sinkevičiūtė

Received: 1 October 2012 / Revised: 6 December 2012 / Accepted: 19 December 2012 / Published online: 6 January 2013

Abstract Thin MoO_2 films were electrodeposited on a selenium pre-deposited SnO_2|glass plate. The photoelectrochemical properties of MoO_2 films were investigated in 0.1 M Na_2SO_4 solution by the ultraviolet–visible spectrophotometry, linear sweep voltammetry, and altering current impedance measurement techniques. It was found that under illumination with the incident light of λ=366 nm, the photo response of the MoO_2|SnO_2|glass electrode resulted from the MoO_2 layer, while the SnO_2 layer served as a sink for photogenerated charge carriers. The MoO_2 film exhibited n-type conductivity. A schematic band structure diagram of MoO_2 in 0.1 M Na_2SO_4 solution was constructed. The flat band potential (E_{fb}), the donor concentration (N_D), the photogeneration current efficiency depended on MoO_2 film thickness. The $[Fe(CN)_6]^{4-/3-}$ redox PEC cell with MoO_2|SnO_2|glass plate as a photoanode was constructed. Power output characteristics such as the open circuit voltage (V_{OC}), short circuit current (I_{SC}), the fill factor (FF), and the light-to-electrical conversion efficiency (η) were determined. The maximum light-to-electrical conversion efficiency exhibited by the PEC cell was 0.94 %.

Keywords MoO_2 film · Photoelectrochemistry · Flat band potential · Band gap diagram

Introduction

The photoelectrolysis [1, 2], photocatalysis [3, 4], and photoelectrochemical power conversion [5] processes have been attracting a considerable interest for decade. The primary problem of these processes is to select an efficient and stable photoelectrode. The selection of semiconductor material is difficult due to the necessity of simultaneously optimizing the semiconductor characteristics such as band gap, the flat band potential, and stability to corrosion. Transition metal oxides today are the most promising semiconductors as the corrosion stability problem both in acidic and alkaline media is basically solved only for these materials. Apart from the corrosion stability requirement, a stable photoelectrode must also exhibit an efficient charge transport through the semiconductor and lower potentials for redox reactions.

The literature survey revealed that the photocatalytic and photoelectrochemical behavior of various transition metal oxides such as TiO_2 [3, 6], WO_3 [4, 7], ZnO [8, 9], CuO [10, 11], and Fe_2O_3 [12] had been well studied. The low solar-to-energy conversion efficiency of these oxides is a major restrict for their practical application, and an urgent search of new materials for a better light to chemical conversion efficiencies is still under investigation.

Nanometric MoO_2 has attracted great technological interest because of its interesting physicochemical properties and is applied as a catalyst [13, 14], an energy storing [15], soft magnetic [16], and optical [17, 18] material.

Recently, electrodeposition has been proposed as an alternative route for the production of MoO_2, and a number of nanostructures, such as nanowires [19, 20], and nanofibers [21], have been synthesized. The composite electrodes based on electrochemically synthesized MoO_2 nanowires possess long-term cycle stability and a specific capacitance as high as 597 $F g^{-1}$ [19]. Electrolytic MoO_2 nanowires offer an alternative substitute for manufacturing Mo-based emitters [20] and can be used as a precursor [21] for the production of Mo nanowires. However, to our knowledge, the MoO_2 film, obtained by electrodeposition, has not yet been characterized for its photoelectrochemical performance.

N. Dukštienė (✉) · D. Sinkevičiūtė
Department of Physical Chemistry,
Kaunas University of Technology, Radvilenu pl,
50524 Kaunas, Lithuania
e-mail: nijole.dukstiene@ktu.lt

It is worth mentioning that photoelectrochemical devices usually require a transparent conducting oxide film as a substrate for collecting electron efficiently. Thus, photoactive semiconductor films are usually grown on SnO_2, indium tin oxide and fluorine doped tin oxide plates.

Recently [22], our group has reported the morphological and optical properties of an amorphous MoO_2 film deposited on SnO_2|glass surface. The results have demonstrated that the MoO_2 film is highly absorbing and shows a direct band to band transition. The band gap energy (E_g) depends on the film thickness and lies within 2.38−2.53 eV. Both its amorphous nature and the direct band gap with a high absorption coefficient make MoO_2 film an ideal candidate as an electrode for photovoltaic and photoelectrochemical solar cells. In addition, MoO_2 is composed of MoO_6 octahedra. A MoO_6 octahedron is often advantageous for photoapplications because the excitation energy can easily migrate in the structure. Therefore, we have considered it of interest to investigate the photoelectrochemical properties of MoO_2 films obtained by electrodeposition.

In the present paper, we continue our recent investigations on the MoO_2 film obtained by electrodeposition and examine its photoelectrochemical behavior in 0.1 M Na_2SO_4 solution. Photoelectrochemical properties such as conductivity type, the current–potential characteristics, the flat band potential (E_{fb}), and the photogeneration current efficiency (IPCE) are discussed.

The MoO_2|SnO_2|glass plate as a photoanode has also been tested in a photoelectrochemical (PEC) cell. The PEC cell electrolyte was $K_4[Fe(CN)_6]/K_3[Fe(CN)_6]$ redox couple in 0.1 M Na_2SO_4 supporting solution. Power output characteristics such as the open circuit voltage (V_{OC}), short circuit current (I_{SC}), the fill factor (FF), and the light-to-electrical conversion efficiency (η) have been determined. The light-to-electrical conversion efficiency of MoO_2 film has been compared with those described in literature for other transition metal oxides.

The obtained results have offered new information, which provides the further insight into MoO_2 film properties.

Experimental

MoO_2 film electrodeposition

A thin MoO_2 film of controlled morphology was electrodeposited by a two-step route on a SnO_2|glass plate, as previously described in our papers [22, 23]. Briefly, a commercially available ISE-2 three-compartment cell and a PI-I-50 potentiostat coupled to a PR programmer (ZIP, Russia) were employed to electrodeposit molybdenum oxide thin films onto initially selenium pre-deposited tin oxide-coated glass plates. The electrolyte solution was 0.2 M Na_2MoO_4 in 0.22 M sodium citrate with the pH value of 8.3. The pH of the electrolyte was adjusted by adding 1 M H_2SO_4 or 6 M NaOH solutions. The electrolysis temperature was 293 K. The counter electrode was a platinum spiral with an active area of 12.5 cm^2. Films were electrodeposited on the Se|SnO_2|glass plate applying −1.0, −1.1, and −1.2 V potentials vs. [Ag|AgCl, $KCl_{(sat)}$] for 30 min. Under potential controlled conditions, the MoO_4^{2-} ions discharge to form the hydrous $MoO_2{\cdot}xH_2O$, which during interaction with the predeposited selenium layer loses molecular water:

$$MoO_2 \cdot xH_2O + e^- \rightarrow MoO_2 + xH_{ads} + xOH^-, \quad (1)$$

$$2H_{ads} + Se \rightarrow H_2Se \quad (2)$$

The obtained plates consist of SnO_2|glass plate covered with a MoO_2 film of different thickness, and throughout the paper, these plates would be labeled as electrodes S. The X-ray diffraction analysis of as-deposited MoO_2 films revealed their amorphous nature.

MoO_2 film characterization

The absorbance ultraviolet–visible (UV–Vis) spectra of the MoO_2|SnO_2|glass plate were recorded using a UV–Vis Spectronic Genesis spectrophotometer (Perkin Elmer Spectrum GX, USA) in the range of 300–1100 nm, and the sampling interval was 1 nm. The reproducibility of the measurements was within approximately ±0.5 %. The spectra were taken using an identical glass plate as a reference.

Photoelectrochemical measurements were performed in a three-compartment photochemical quartz cell connected to a computer-controlled Autolab PGSTAT12 (Ecochem, The Netherlands) potentiostat/galvanostat equipped with GPES and FRA 4.9 software. The electrolyte was 0.1 M Na_2SO_4 solution. A MoO_2|SnO_2|glass plate (electrode S) was used as a working electrode, and the active area of MoO_2 film was 1.65 cm^2. The electrical contact was made to the uncoated part of the SnO_2 surface. A platinum spiral with the active area of 12.5 cm^2 and an Ag|AgCl, $KCl_{(sat)}$ electrode were used as a counter and reference electrodes, respectively. Throughout the paper, all potential values are referred to this reference electrode. The area of MoO_2 was carefully positioned under UV illumination. A UV lamp with λ_{max}= 366 nm (F8W/BLB, General Electric) was placed at a distance of 1 cm from electrode S surface and was used as the illumination source. Since the transmittance of incident light of 366 nm through the pure glass plate was very low, the front side illumination was applied. The incident light intensity was evaluated by potassium ferrioxalate actinometry [24]. The average power density at 366 nm was calculated to

be 1.8 mW cm^{-2}. During measurements, the cell was placed inside a dark box to eliminate the influence of sight light. The measurements were performed at room temperature. Only freshly prepared solutions were used for measurements and were not deaerated during the experiments. The altering current impedance measurements were carried out at the frequency of 1 kHz in the dark. The current signal amplitude was 0.008 V_{rms}.

The $MoO_2|SnO_2|$glass plate as a photoanode was tested in a photoelectrochemical cell. The light source was UV lamp with λ_{max}=366 nm (F8W/BLB, General Electric). The average power density at 366 nm was calculated to be 1.8 mW cm^{-2}. The PEC cell electrolyte was a ferro-ferricyanide redox couple in 0.1 M Na_2SO_4 supporting solution. The concentrations of $K_4[Fe(CN)_6]$ and $K_3[Fe(CN)_6]$ in PEC cell were 0.01 and 0.01 M or 0.005 and 0.01 M, respectively.

All solutions were prepared using doubly distilled water and analytical grade reagents. SeO_2 (>99 %, Reachim, Russia), Na_2MoO_4 $2H_2O$ (>99 %, Sigma-Aldrich, Germany), sodium citrate ($C_6H_5Na_3O_7$ $2H_2O$) (>99 %, Lachema, Czech Republic), acetone (C_3H_6O) (>99 %, Standard, Poland), HNO_3 (65 %, Penta, Czech Republic), H_2SO_4 (96 %, Barta a Cihlar, Czech Republic), Na_2SO_4 (>99 %, Lach-Ner, Czech Republic), NaOH (>99 %, Standard, Poland), $K_4[Fe(CN)_6]$ (>99 %, Reachim, Russia), and $K_3[Fe(CN)_6]$ (>99 %, Reachim, Russia) were used as received.

Results and discussion

Optical characteristics of electrodes S

The layered $MoO_2|SnO_2|$glass plate can be considered either as a photoelectrode having an abrupt or a grated band gap junction between the MoO_2 and SnO_2 interface.

The electrode S prepared by electrodepositing MoO_2 film on a $SnO_2|$glass plate from 0.2 M Na_2MoO_4 in 0.22 M sodium citrate solution a applying definite −1.0, −1.1, and −1.2 V potential throughout the paper are labeled as S_1, S_2, and S_3, respectively (Table 1).

The morphological and optical properties of an individual MoO_2 film of each electrode S have been discussed in our previous paper [22] and herein are summarized in Table 1.

The absorption spectra of an individual $SnO_2|$glass plate and electrodes S_1, S_2, and S_3 are shown in Fig. 1.

As one can see, the $SnO_2|$glass plate weakly responds to excitation of UV incident light (Fig. 1, curve 1) and is transparent in the visible range. In contrast, the electrodes S are highly absorbing in the UV spectral region. For example, the absorbance of the $SnO_2|$glass plate at λ= 366 nm is 0.117, while the absorption of the electrodes S_1, S_2, and S_3 is 0.501, 1.074, and 0.749, respectively.

The optical band gap energy (E_g) of a semiconductor electrode is a very important parameter in solar energy conversion systems. Only photons of equal or higher energy than the band gap energy will be absorbed by the semiconductor film.

Depending on the synthesis method, the band gap energy values of a SnO_2 film lay within 2.5–4.1 eV range [25–28].

In the light of a considerable scattering in the reported data, we determined the band gap energy of the SnO_2 film.

The optical band gap of semiconductor material is characterized by Tauc equation [29]:

$$\alpha = \frac{B\left(h\nu - E_g\right)^r}{h\nu}, \tag{3}$$

where B is an inverse proportion to the width of the conduction band and the valence band tail, $h\nu$ is the photon energy (eV), E_g is the optical band gap (eV), and r characterizes the transition type. The values of r are 1/2 and 2 for direct and indirect allowed transitions, respectively.

The optical absorption coefficient α of the SnO_2 film was calculated by the following equation [30]:

$$\alpha = 2.303\frac{A}{d} \tag{4}$$

where d is the SnO_2 film thickness and equals 1×10^{-4} cm, and A is absorption.

The values of absorption coefficients were in the order of 10^3 cm^{-1} throughout the wavelength region studied.

Table 1 Electrode labeling, deposition potential, and characterization of MoO_2 film on $SnO_2|$glass plate

Electrode	MoO_2 film deposition potential (V)	Average thickness of film (nm)	Morphological characteristics [22]			Optical constants [22]		
			Root means square roughness (nm)	Grains		Absorption coefficient[a] $\alpha\times10^{-4}$ (cm^{-1})	Band gap energy (eV)	Urbach energy (eV)
				Maximum height (nm)	Average width (nm)			
S_1	−1.0	100	26	200	560	8.98	2.53	0.29
S_2	−1.1	460	14.2	65.5	543	6.69	2.42	0.45
S_3	−1.2	600	8.9	93.2	351	3.65	2.38	0.37

[a] Absorption coefficient corresponding to λ=366 nm

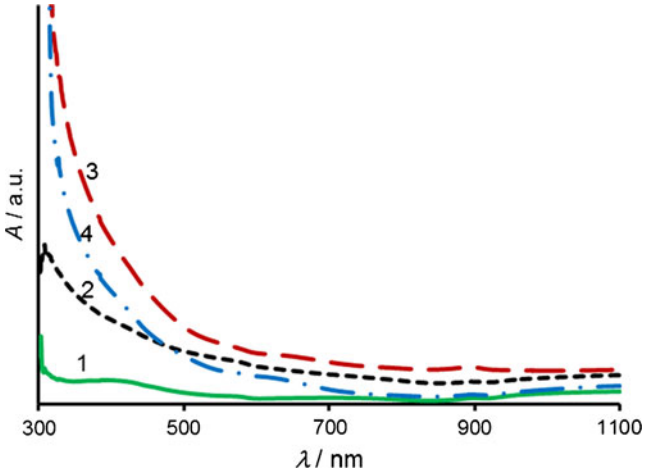

Fig. 1 UV–Vis absorption spectra: *1* SnO_2|glass plate; *2* electrode S_1; *3* electrode S_2; *4* electrode S_3

The optical band gap value of the SnO_2 film was determined by replotting the corresponding UV–Vis absorption spectrum (Fig. 1, curve 1) data to the $(\alpha hv)^2$ or $(\alpha hv)^{1/2}$ dependence as a function of the photon energy *hv*. The experimental data fit better the straight line plot near the fundamental absorption edge in the $(\alpha hv)^2$ vs. *hv* dependence. Extrapolation of the linear part of plot to $(\alpha hv)^2=0$ gave the direct band gap value of 4.07 eV. The E_g value obtained for SnO_2 was close to that reported in [27]. Thus, only the incident light of a wavelength equal to or shorter than 305 nm would activate the SnO_2 film in photoelectrochemical applications.

The reduced band gap energy and a higher absorption coefficient of the MoO_2 film (Table 1) as compared to these of SnO_2 predict that the dominant absorption in the electrode S comes from the MoO_2 film.

The light penetration depth ($1/\alpha_\lambda$) to which incident light of λ=366 nm penetrates into the MoO_2 film was estimated to be 110, 149, and 273 nm for the electrodes S_1, S_2, and S_3, respectively. The majority of incident light would be absorbed by the whole MoO_2 film only for the electrode S_1. This results in a nearly uniform concentration of charge carriers through the film. In the case of electrodes S_2 and S_3, it is only the top of 149 and 273 nm, respectively, which absorbs the majority of incident light. The MoO_2 film beyond the penetration depth does not significantly contribute to light absorption and consequently to the generation of charge carriers. The highest concentration of photogenerated charge carriers would be produced in the top layer of the MoO_2 film.

The above results allow concluding that in the MoO_2|SnO_2|glass plate the majority of incident light of 366 nm would be absorbed by the MoO_2 layer, while the SnO_2 layer is a window layer transparent to its wavelength. The photoexcitement would photogenerate charge carries in the MoO_2 film, while the SnO_2 layer would serve as a sink for charge carriers.

Photoelectrochemical performance of electrode S

A significantly negative shift of the electrode S open circuit potential (E_{OCP}) in 0.1 M Na_2SO_4 electrolyte under UV illumination as compared to that without illumination (Table 2) indicates that photoelectrons and photoholes are effectively separated.

Representative linear sweep voltammograms of S_1 and S_3 electrodes in 0.1 M Na_2SO_4 electrolyte are presented in Fig. 2a and b, respectively. In order to ensure the least perturbation to the equilibrium, a slow potential scan of 2 $mV\,s^{-1}$ was applied starting from E_{OCP} to anodic direction up to 1.4 V.

In the acidic electrolyte, the hydrogen evolution reaction on the MoO_2 surface starts at the potentials more negative than −0.4 V, and the redox transition of Mo^{4+} to Mo^{6+} occurs at the potentials around 0.2 V [31]. In the neutral and alkaline solutions, MoO_2 dissolves to MoO_4^{2-} at the rate depending on pH [32].

The cathodic current flow under dark conditions at approximately E=0 V (Fig. 2a, b, curves 1) is attributable to hydrogen ion adsorption / intercalation by the reaction:

$$MoO_2 + xH_3O^+ + xe^- \rightarrow MoO_{2-x}(OH)_x \cdot xH_2O \qquad (5)$$

The cathodic currents for a thicker MoO_2 film electrode maintained the same magnitude at the negative potentials under UV illumination (Fig. 2 b, curve 2), thus demonstrating the independence of the adsorption / intercalation process (Eq. 5) on illumination. Interestingly, on a thinner MoO_2 film (Fig. 2 a, curve 2), this process starts at more negative potentials.

The absence of any anodic features under dark polarization conditions indicates that the MoO_2 film deposited on SnO_2|glass plate is stable and does not dissolve in 0.1 M Na_2SO_4 electrolyte. The sharp current increase at a potential of approximately 1.2 V is related to the electrochemical oxidation of water molecules.

Both the increase in anodic current and the potential shift towards more negative values under illumination indicate the electrodes S to possess the n-type conductivity.

Table 2 Open circuit potential values of electrodes S and SnO_2|glass plate in the dark and under illumination in 0.1 M Na_2SO_4 electrolyte solution

Electrode	E_{OCP} (V)	
	Dark	Illumination
SnO_2	0.00	0.00
S_1	−0.20	−0.62
S_2	−0.18	−0.49
S_3	−0.17	−0.37

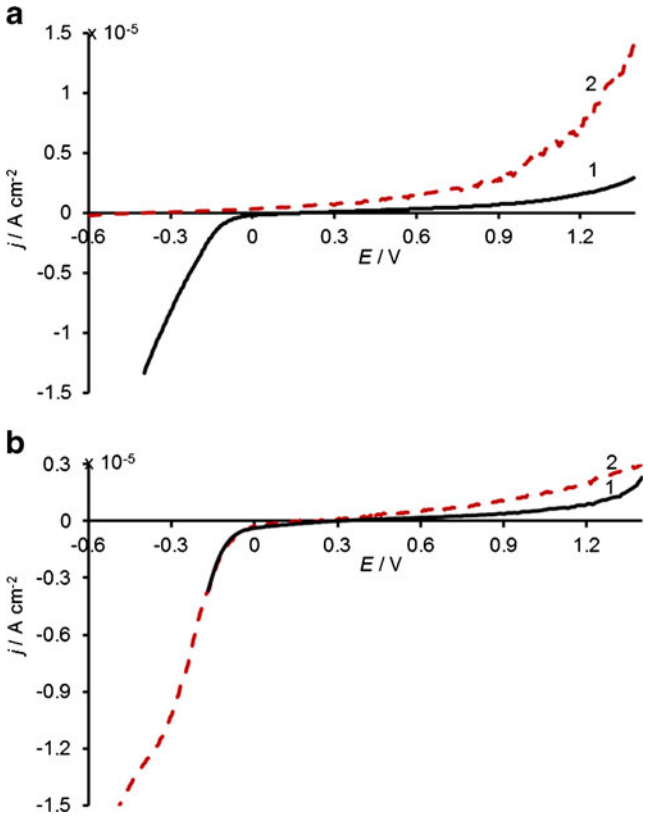

Fig. 2 Linear sweep voltammograms of electrode S in 0.1 M Na_2SO_4 electrolyte: *1* in the dark, *2* under illumination. **a** S_1; **b** S_3

When the area of a counter electrode is sufficiently larger, the photo response of the working electrode depends on (1) the rate of oxygen reduction reaction, (2) the number of electron–hole pairs generated in the semiconductor; and (3) the kinetic of electron transport to the back contact of the electrode.

As one can see in Fig. 2, the photocurrents increased steeply with the applied potential and no limiting current was attained. This indicates that (1) the electron transport in the whole MoO_2 film controls the overall photo characteristics and (2) the electron transport rate inside the film does not reach the level comparable to the rate of photohole capture at the solution electrode interface (SEI).

The photocurrent density (j_{ph}) was calculated as a difference between the linear sweep voltammetric response of an electrode in the dark and that under illumination. The representative value of photocurrent density for each electrode S at E=1.0 V is given in Table 3. The anodic photocurrent density is strongly influenced by the MoO_2 film thickness. Although all electrodes S show a high absorption (Fig. 1), relatively low photocurrent densities were generated. The highest anodic photocurrent densities were registered for the electrode S_1.

The decrease in photocurrent density may be explained by two competitive factors: (1) the light penetration depth ($1/\alpha_\lambda$) and (2) recombination rate losses at the defect centres in the amorphous MoO_2 film network.

Under illumination, photoelectrons are excited from the valence band to the conduction band of the MoO_2 film and then should be transported to the MoO_2/SnO_2 interface. The transfer rate of the photoelectrons depends on the concentration gradient and the number and energy distribution of recombination centres. Hence, the photocurrent density depends on the amount of electrons collected by the SnO_2 layer.

As discussed above, only for electrode S_1 the majority of UV incident light would be absorbed by the whole MoO_2 film, resulting in a nearly uniform concentration of charge carriers through the film. Besides, the rough surface area of the electrode S_1 provides for a larger contact area between the electrode and the electrolyte solution, which is also beneficial for the photogenerated carrier transfer. On the contrary, for electrodes S_2 and S_3 beyond the light penetration depth, MoO_2 does not significantly contribute to light absorption and thus to the generation of charge carriers. In such a case, the majority of charge carriers and consequently the highest concentration gradient of photogenerated electrons are produced in the top layer of the MoO_2 film. As a result, the photoelectrons should be transported through an amorphous network of the MoO_2 film to the SnO_2 layer for more than 300 nm — an impressive distance for such a fairly high band gap semiconductor. On the way through the whole MoO_2 film to the SnO_2 layer, the photoelectrons and photoholes have a greater tendency to recombine, and the photocurrent density decreases with the film thickness. The higher Urbach energy of a thicker MoO_2 film as compared with thinner ones (Table 1) indicates a higher concentration of structural defects in thicker films. The photogenerated electrons could be partially trapped by these defects rapidly, owing to the formation of a Schottky barrier and band-bending at the $MoO_2|SnO_2$/electrolyte interface, which additionally suppresses the enhancement of photocurrent density.

Therefore, it could be concluded that the highest photocurrent on the electrode S_1 results from the nearly uniform concentration of photogenerated electrons and a larger contact area between the MoO_2 film and 0.1 M Na_2SO_4 solution.

The anodic photocurrents were fitted according to a power low [33]:

$$(j_{ph})^n \infty (E - E^*) \tag{6}$$

where E is the electrode potential (V), j_{ph} is photocurrent density ($A cm^{-2}$), E^* is the extrapolated zero photocurrent potential, which can be assumed as a reasonable estimate of the flat band potential (V), and n is the fitting exponent.

Table 3 Photoelectrochemical characteristics of electrodes S in 0.1 M Na_2SO_4 electrolyte solution

Electrode	$j_{ph}\times10^6$ at E=1.0 V ($A cm^{-2}$)	Fitting results of anodic photocurrents to expression of power low (Eq. 6)		Fitting results of capacitance data to expression of low band-bending (Eq. 8)			IPCE (%)
		n	E^* (V)	ψ_c	E_{fb} (V)	$N_D\times10^{-20}$ (cm^{-3})	
S_1	3.18	0.395	−0.63	0.33	−0.515	2.98	0.57
S_2	1.45	0.342	−0.49	0.15	−0.495	2.28	0.26
S_3	0.81	0.642	0.10	0.33	−0.502	9.98	0.15

Figure 3 shows the best fitting results of voltammogram for each electrode S, under illumination. The best linear regression was observed with the values of $n<1$. The disclosed supralinear behavior ($\frac{1}{n}>1$) in the investigated potential range confirms the presence of surface and bulk recombination phenomena involving the photogenerated carriers as well as the geminate recombination effects generally occurring in the amorphous film [33]. Geminate recombination phenomenon is typical for materials containing a non-zero density of localized states near Fermi level. The representative values of n and E^* obtained from the best fitting results for each electrode S are reported in Table 3.

The quantitative measure of semiconductor photoelectrochemical properties is the incident photon-to-current efficiency (IPCE) [34]:

$$\mathrm{IPCE}\ (\%) = 100\frac{1,240 j_{ph}}{\lambda P_o}, \tag{7}$$

where j_{ph} is the photocurrent density ($mA cm^{-2}$), λ is the wavelength of the incident light (nm), and P_o is the incident light power density ($mW cm^{-2}$).

The calculated value of the IPCE for each electrode S is presented in Table 3.

The flat band potential (E_{fb}) at which there is no net transfer of charge and the band-bending is reduced to zero in the semiconductor electrode is a property of the specific SEI.

The E_{fb} potential for electrodes S was determined from the capacitance measurements in the dark. Most generally, the flat band potential and density of states (N_D) in a specific electrochemical system are determined from the well-known linear Mott–Shottky plot [35]. In fact the Mott–Shottky theory assumes a well-defined long-range order of semiconductor with clearly distinguishable energy band gaps.

Our recent examination of MoO_2 films [23] revealed their amorphous nature. It is expected that Mott–Schottky plots will deviate from a linear relationship because of the multiple donor levels, which result from structural defects, grain boundaries, and dislocations in amorphous oxide. In this case, the concentration of donors increases with increasing electrode potential as the Fermi level shifts down from conduction band to valence band [36]. Therefore, a number of workers [36–38] modeled Mott–Schottky theory by assuming consecutive ionization of donor levels and by utilizing the Euler method [39]. Other scientists [40], however, further pointed out that the semiconductor model is helpful to understand the electronic properties and is applicable for a period of time in which the donor concentration is approximately constant. Thus, the Mott–Schottky analysis can be used for amorphous oxide films as long as no major changes occur. Against, Di Quarto et al. [41] proposed a model for the interpretation of the impedance responses of anodic semiconductor oxides by applying the amorphous semiconductor theory formulated by Cohen and Lang [42].

In spite of the numerous studies on amorphous metal oxide/electrolyte interface, a general acceptance of interpretative model is still lacking. Therefore, we decided from a phenomenological point of view to use the model proposed by Di Quarto et al. [41] in this work. This model was applied for interpretation of amorphous metal oxide-electrolyte interface in [35, 43].

According to the model, proposed by Di Quarto, the total capacitance, under hypothesis of a constant density of states, at low band-bending conditions is defined by the following expression [41]:

$$C(\omega,\ \psi_s) = \sqrt{\varepsilon\varepsilon_0 e^2 N_D}\left(1+\ln\frac{\psi_s}{\psi_c}\right)^{-1} \tag{8}$$

where C_s is space charge capacitance (F), ε_o is the permittivity of vacuum, ε is the permittivity of the semiconductor, e is the charge of electron, N_D is the density of states (cm^{-3}), and $\psi_s=E\text{-}E_{fb}$ is the band-bending.

For high band-bending conditions, the following analytical expression for the total capacitance was derived [41]:

$$\frac{1}{C(\omega,\ \psi_s)} = \frac{1}{\sqrt{\varepsilon\varepsilon_0 e^2 N_D}} \times\left(\ln\frac{\psi_g}{\psi_c}+\sqrt{1+\frac{2}{\psi_g}\left(\psi_s-\psi_g\right)}\right) \tag{9}$$

where $\psi_g=(E_g/2-E_F)$ is the potential corresponding to the intersection point of the midgap with the Fermi level.

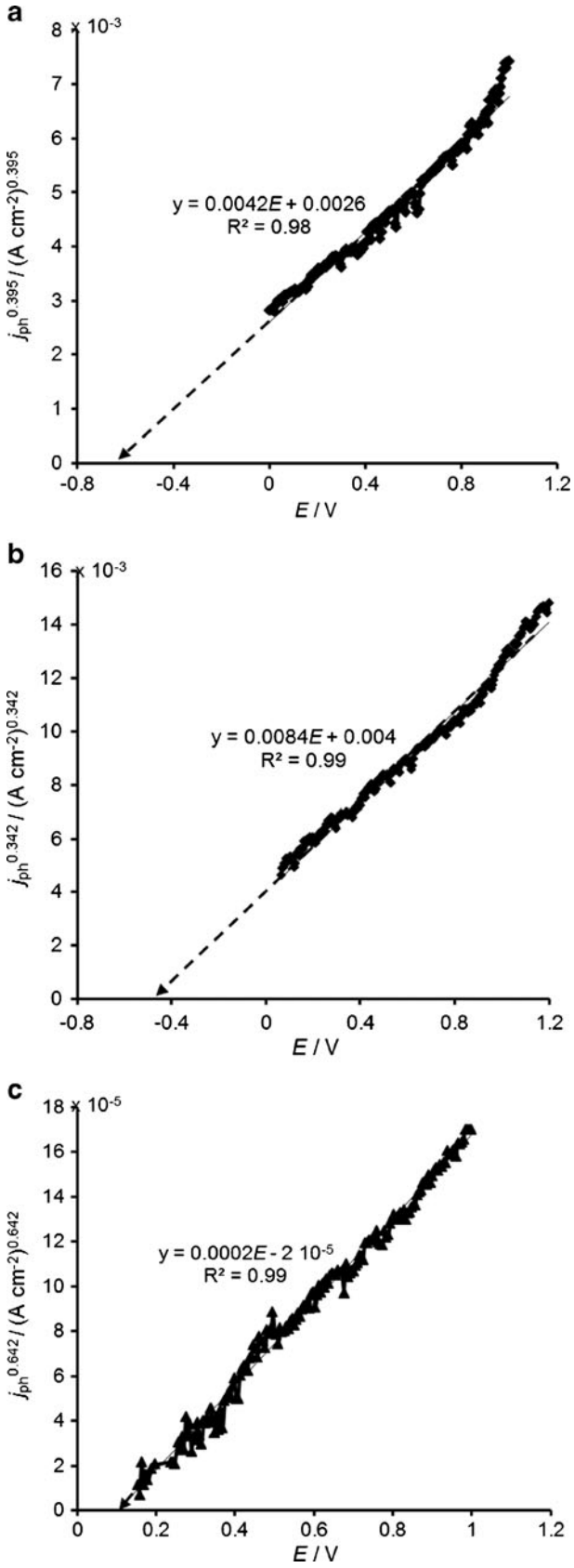

Fig. 3 Dependance j_{ph}^{n} on applied potential of electrode S in 0.1 M Na_2SO_4 electrolyte. **a** S_1; **b** S_2; **c** S_3

A reasonable reproduction of the experimental capacitance data for each electrode S was obtained fitting according to (Eq. 8). The experimental C^{-1} vs. E plots for each electrode S (points) and plots obtained for the best fitting of experimental results (lines) to expression of low band-bending (Eq.8) are shown in Fig. 4. The representative parameters of ψ_c, E_{fb}, and N_D obtained from the best fitting results for each electrode S are given in Table 3. The permittivity (ε) of the MoO_2 film was assumed to be $9.5 \times \varepsilon_o$ [44].

Notably, the highest concentration of N_D in the electrode S_3 (Table 3) could offer the low resistivity of the MoO_2 film, which is favorable for photoelectron transfer. However, the lowest photocurrent densities generated on the electrode S_3 (Table 3) imply that the ratio of the effect on the light penetration depth and the concentration of structural defects to the effect of the MoO_2 film resistance in this electrode might be comparable.

It should be noted that the potential of zero photocurrent of electrode S_3 is positive by several hundred millivolts than that obtained from capacitance measurements analysis (Table 3). It can be explained by the presence of localized states and/or surface states situated deep in the band gap.

The photoactivity of a semiconductor electrode is determined not only by its band gap energy but also by the position of the valence and conduction bands relatively to the hydrogen and oxygen evolution potentials. The energetic position of these band edges is determined by the chemistry of the SEI which, in turn, is controlled by the composition of the electrode, the nature of the surface and the electrolyte composition.

The schematic representation of band gap structure diagram of each electrode S in 0.1 M Na_2SO_4 (Fig. 5) was built

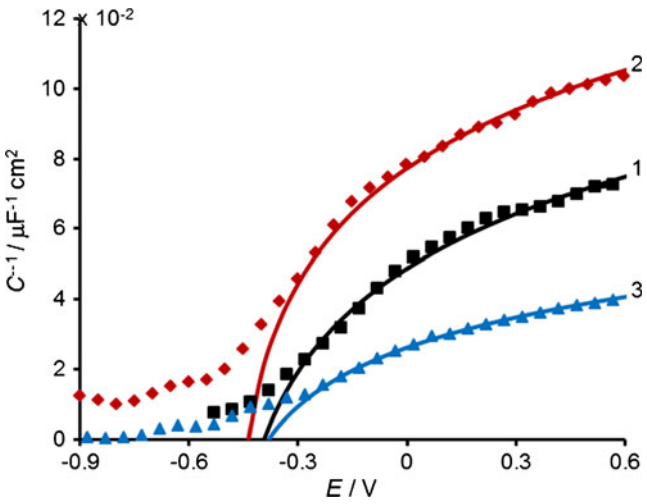

Fig. 4 Experimental dependence (points) of the inverse capacitance of electrode S in 0.1 M Na_2SO_4 electrolyte. *1* S_1; *2* S_2; *3* S_3. *Lines* denote curves obtained by fitting experimental curve to low band-bending Eq. 8

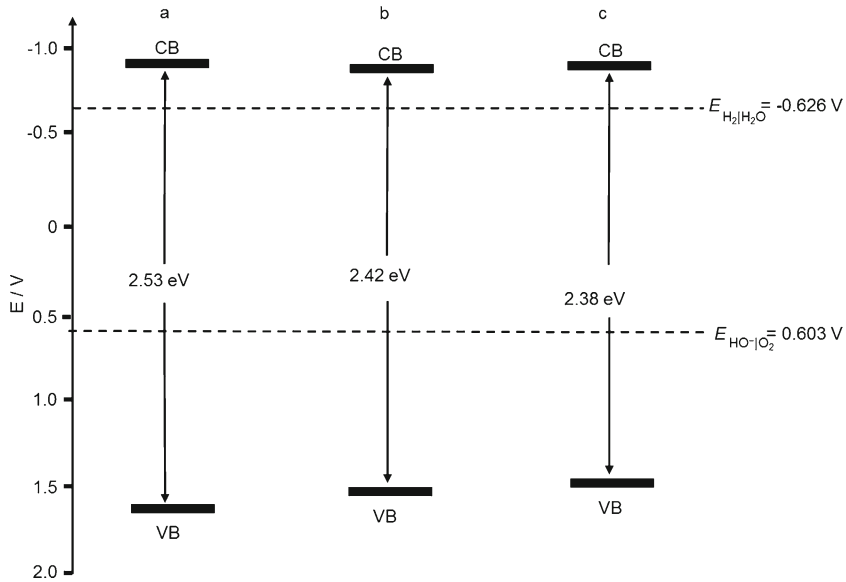

Fig. 5 Schematic representation of band gap structure diagram built for electrode S in 0.1 M Na_2SO_4 electrolyte at pH 6.33. **a** S_1; **b** S_2; **c** S_3

assuming the flat band-bending conditions. When energy bands are flat the Fermi level (E_F) corresponds to the flat band potential. The values of E_{fb} obtained from the best fitting results (Table 3) were used for diagrams drawing. The conduction band mobility edge (E_{CB}) by analogy with ($E_{CB}-E_F$) values reported for amorphous metal oxide films [43, 45, 46] was assumed to be approximately 0.4 eV above the E_F.

The location of valence band mobility edge (E_{VB}) was calculated from optical band gap (E_g) by the following equation:

$$E_g = E_{CB} - E_{VB} \quad (10)$$

In 0.1 M Na_2SO_4 solution, the valence band energy level of electrode S_1 is the lowest in comparison with the other electrodes S studied, indicating the most powerful oxidation capacity of photogenerated holes. The conduction band energy is approximately at the same level for all electrodes S, implying a similar reductive capacity of the photoelectrons. MoO_2 film has a conduction band edge position at the energy level just above the reversible potential of the H^+/H_2O redox couple.

It is nothing to mention here that the capacitance data fitting procedure was carried out based on the hypothesis of constant carries density. Additional studies are necessary to obtain a deeper understanding of characteristic energy levels of the amorphous MoO_2 film/electrolyte junction.

The experimental results discussed above indicate that the electrode S_1 shows the best photoelectrochemical properties among the other electrodes S studied. Therefore, this electrode was chosen for the further characterization in a PEC cell. On the basis of the band gap structure diagram of the $MoO_2|SnO_2|$glass electrode S_1 (Fig. 5 a), the PEC was focused on the $[Fe(CN)_6]^{4-/3-}$redox couple. The ferro-ferricyanide redox couple is one of the few redox couples demonstrating a compatible with effective oxidative photoelectrochemistry in several semiconductors [47].

A PEC cell with the configuration of the electrode S_1 | 0.1 M Na_2SO_4, $[Fe(CN)_6]^{4-/3-}$ | Pt was formed. The photocurrent–voltage curves of the PEC cell are illustrated in Fig. 6. No attempt was made to optimize the power output characteristics, and the presented data only serve for characterizing the $MoO_2|SnO_2|$glass electrode.

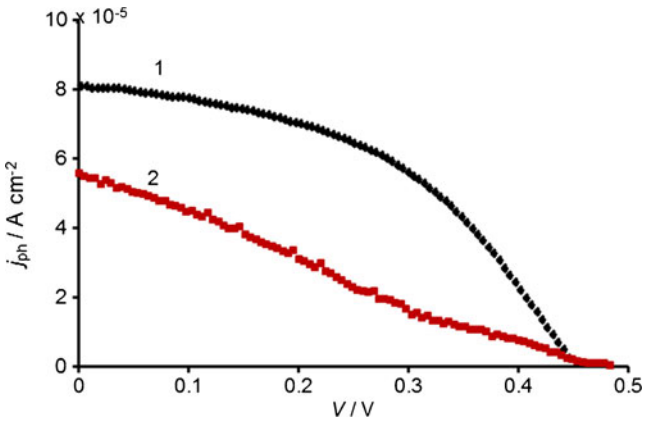

Fig. 6 Photocurrent–voltage curves for electrode S_1 in PEC cell of different xM$[Fe(CN)_6]^{4-}/y$M $[Fe(CN)_6]^{3-}$ redox couple concentration: *1* x=0.01 and y=0.01; *2* x=0.005 and y=0.01

Table 4 Power output characteristics of photoelectrochemical cells

Electrolyte concentration $\times K_4[Fe(CN)_6]/y K_3[Fe(CN)_6]$	$I_{SC}\times10^5$ (A cm^{-2})	$I_{MP}\times10^5$ (m^{-2})	V_{OC} (V)	V_{MP} (V)	FF	η (%)
0.01 M/0.01 M	8.11	5.90	0.452	0.286	0.460	0.94
0.005 M/0.01 M	5.56	3.71	0.479	0.157	0.219	0.32

The fill factor (FF) is essentially a measure of the PEC cell quality and was calculated by the following equation [48]:

$$FF = \frac{V_{MP} \cdot I_{MP}}{V_{OC} \cdot I_{SC}} \quad (11)$$

where V_{OC} is the open circuit potential (V), I_{SC} is the short-circuit current density (Acm^{-2}), I_{MP} is the maximum current at the maximum power output point (Acm^{-2}), and V_{MP} is the maximum voltage at the maximum power output point (V).

The light-to-electrical conversion efficiency in a PEC cell is given [48]:

$$\eta = \frac{FF \times I_{SC} \times V_{OC}}{P_o} \times 100\% \quad (12)$$

The power output characteristics for each PEC cell are shown in Table 4.

Since the ultimate goal of the PEC cell research is to design and develop a system working efficiently under the illumination, the 0.94 % efficiency obtained in this work for the MoO_2 film is an appreciable value.

The light-to-electrical conversion efficiency of the MoO_2 film is considerably lower than that of TiO_2 [6]; however, it is comparable to these of other transition metal oxides [8, 9, 11, 12].

Conclusions

The photo response of the $MoO_2|SnO_2|$glass electrode in 0.1 M Na_2SO_4 solution under illumination with the incident light of λ=366 nm arose from the MoO_2 film, while the SnO_2 layer served as a sink for photogenerated charge carriers.

The MoO_2 film exhibited the n-type conductivity. The flat band potential (E_{fb}), the donor concentration (N_D), the photogeneration current efficiency (IPCE) depended on MoO_2 film thickness. The MoO_2 film 100 nm thick exhibited the best photoelectrochemical characteristics.

The $MoO_2|SnO_2|$glass electrode as a photoanode was a tested in PEC cell with ferro-ferricyanide redox electrolytes. The maximum short circuit current (I_{SC}), open circuit voltage (V_{OC}), and light-to-electrical conversion efficiency (η) of the PEC cell were found to be $8.11 \times 10^{-5} Acm^{-2}$, 0.52 V, and 0.94 %, respectively.

References

1. Nian JN, Hu CC, Teng H (2008) Int J Hydrogen Energy 33:2897–2903
2. Marsen B, Cole B, Miller EL (2008) Sol Energ Mat & Sol Cells 92:1054–1058
3. Mu R, Xu Z, Li L, Shao Y, Wan H, Zheng S (2010) J Hazard Mater 176:495–502
4. Qamar M, Gondal MA, Yamani ZH (2009) Catal Comm 10:1980–1984
5. Nikale VM, Shinde SS, Babar AR, Bhosale CH, Rajpure KY (2011) Sol Energy 85:325–333
6. Fan K, Peng T, Chai B, Chen J, Dai K (2010) Electrochim Acta 55:5239–5244
7. Li W, Li J, Wang X, Ma J, Chen Q (2010) Int J Hydrogen Energy 35:13137–13145
8. Hsu CH, Chen DH (2011) Int J Hydrogen Energy 36:15538–15547
9. Qin Z, Huang Y, Qi J, Li H, Su J, Zhang Y (2012) Solid State Sci 14:155–158
10. Yao MH, Tang YG, Zhang L, Yang HH, Yan JH (2010) Trans Nonferrous Met Soc China 20:1944–1949
11. Chiang CY, Aroh K, Franson N, Satsangi VR, Dass S, Ehrman S (2011) Int J Hydrogen Energy 36:15519–15526
12. Schrebler RS, Altamirano H, Grez P, Herrera FV, Muñoz EC, Ballesteros LA, Córdova RA, Gómez H, Dalchiele EA (2010) Thin Solid Films 518:6844–6852
13. Marin-Flores OG, Ha S (2009) Appl Catal A Gen 352:124–132
14. Al-Kandari H, Mohamed AM, Al-Kharafi F, Zaki MI, Katrib A (2012) Appl Catal A Gen 417–418:298–305
15. Liang Y, Yi Z, Yang S, Zhou L, Sun J, Zhou Y (2006) Solid State Ionics 177:501–505
16. Ma YR, Tsai CC, Lee SF, Cheng KW, Liou Y, Yao YD (2006) J Magn Magn Mater 304:e13–e15
17. Liu X, He Y, Wang S, Zhang Q (2011) J Alloys Compd 509:S408–S411
18. Buono-Core GE, Cabello G, Klahn AH, Lucero A, Nuñez MV, Torrejón B, Castillo C (2010) Polyhedron 29:1551–1554
19. Gao F, Zhang L, Huang S (2010) Mater Lett 64:537–540
20. Wang F, Lu B (2009) Physica B Condensed Mater 404:1901–1904
21. Zach MP, Inazu K, Ng KH, Hemminger JC, Penner RM (2002) Chem Mater 14:3206–3216
22. Dukstiene N, Sinkeviciute D, Guobiene A (2012) Cent Eur J Chem 10:1106–1118
23. Sinkeviciute D, Baltrusaitis J, Dukstiene N (2011) J Solid State Electrochem 15:711–723
24. Calvert JG, Pitts JG (1966) Photochemistry. Wiley, New York
25. Reddaway SF, Wright DA (1965) Br J Appl Phys 16:195–198
26. Stanimirova TJ, Atanasov PA, Dimitrov IG, Pikovska AO (2005) J Optoeklectron Advanced Mater 7:1335–1340
27. Sharma A, Tomar M, Gupta V (2011) Sens Actuators B Chemical 156:743–752
28. Zakrzewska K, Radecka M, Przewoznik J, Kowalski K, Czuba P (2005) Thin Solid films 490:101–107
29. El-Samanoudy MM (2003) Thin Solid Films 423:201–211
30. Halimah MK, Daud WM, Sidek HAA, Zaidan AW, Zainal AS (2010) Mater Sci-Poland 28:173–180
31. Rajeswari J, Kishore PS, Viswanathan B, Varadarajan TK (2009) Electrochem Commun 11:572–575
32. Badaway WA, Al-Kharafi FM (1998) Electrochim Acta 44:693–702
33. Santamaria M, Di Quarto F, Habazaki H (2008) Electrochim Acta 53:2272–2280
34. Mintsouli I, Philippidis N, Poulios I, Sotiropoulos S (2006) J Appl Electrochem 36:463–474
35. Muñoz AG (2007) Electrochim Acta 52:4167–4176
36. Lee EJ, Pyun SI (1992) J Appl Electrochem 22:156–160
37. Pyun SI, Kim CH (1991) Int J Hydrogen Energy 16:661–664
38. Dean MH, Stimming U (1989) Corrosion Sci 29:199–211
39. Daniels RW (1978) An introduction to numerical methods and optimization techniques. North-Holland, New York

40. Schultze JW, Lohrengel MM (2000) Electrochim Acta 45:2499–2513
41. Di Quarto F, La Mantia F, Santamarıa M (2005) Electrochim Acta 50:5090–5102
42. Cohen JD, Lang DV (1982) Phys Rev B 25:5321–5350
43. Muñoz AG, Staikov G (2006) J Solid State Electrochem 10:329–336
44. Ramesh CK, Reddy VR, Choi CJ (2004) Mater Sci Eng B 112:30–33
45. Piazza S, Calà L, Sunseri C, Di Quarto F (1997) Ber Bunsenges Phys Chem 101:932–942
46. Santamaria M, Di Quarto F, Habazaki H (2008) Corrosion Science 50:2012–2020
47. Hilal HS, Ismail RMA, El-Hamouz A, Zyoud A, Saadeddin I (2009) Electrochim Acta 54:3433–33440
48. Yadav AA, Masumdar EU (2010) Sol Energy 84:1445–1452